Article

Effect of Tempering Temperature on Microstructure and Intergranular Corrosion Property of 2205 Duplex Stainless Steel

Xianfu Luo [1], Kun Fang [1], Wenli Zhang [1], Jinmin Zhang [1], Xiao Yang [1,2,*], Xiaoyong Liu [1,2], Xiaoqin Zha [1,2,3] and Xinyao Zhang [1,2,3]

[1] Luoyang Ship Material Research Institute, Luoyang 471023, China; luoxf_725@126.com (X.L.); fangkun2006@126.com (K.F.); zhangwenli_725@163.com (W.Z.); zhangjinmin@126.com (J.Z.); liuxiaoyongsjtu@163.com (X.L.); zha1687827905@163.com (X.Z.); 13525971194@163.com (X.Z.)

[2] State Key Laboratory for Marine Corrosion and Protection, Luoyang 471023, China

[3] Henan Key Laboratory of Technology and Application of Structural Materials for Ships and Marine Equipments, Luoyang 471023, China

* Correspondence: y19850419h@126.com

Abstract: The effect of tempering temperature on the microstructure and intergranular corrosion property of 2205 duplex stainless steel (DSS2205) was determined using a boiling acid intergranular corrosion test (boiling 65% nitric acid and 50% sulfuric acid–ferric sulfate), an optical microscope, a transmission electron microscope, and a double-loop electrochemical potentiokinetic reactivation (DL-EPR) test. The results show that the ferrite content of the DSS2205 is about 50% in a specimen close to a solid solution state (1050 °C for 1 h, then water-quenched) when tempered at 675 °C–725 °C for 1 h. As the tempering temperature rises to 750 °C–800 °C for 1 h, the ferrite content drops gradually from 49% to 35%. $M_{23}C_6$, FeCr (σ phase), and Cr_2N phases are precipitated when the specimen is tempered at 675 °C–800 °C for 1 h. When the tempering temperature rises to 750 °C–800 °C for 1 h, the content and size of σ phase increase significantly. In the boiling acid intergranular corrosion test, when the specimen is tempered at 675 °C–725 °C for 1 h, the corrosion rate is higher than when it is tempered at 750 °C–800 °C for 1 h. In the DL-EPR test, when the specimen is tempered at 675 °C–800 °C for 1 h, the intergranular corrosion sensitivity rises gradually. External polarization is added during the DL-EPR test, and the test principle is different from that of the boiling acid intergranular corrosion test, resulting in a different sensitivity to intergranular corrosion compared to boiling acid intergranular corrosion.

Keywords: tempering temperature; 2205 duplex stainless steel; microstructure; corrosion property

1. Introduction

As a typical, representative second-generation duplex stainless steel, 2205 duplex stainless steel (DSS2205) is widely used in the petroleum, chemical, marine engineering, construction, and other industries. It has the advantages of austenitic stainless steel and ferritic stainless steel and has high strength and good corrosion resistance. When the ratio of two phases is close to 1:1, duplex stainless steel exhibits the best comprehensive performance [1–3]. After an improper heat treatment (such as sensitization), the two-phase ratio of dual-phase steel will change, and second phases such as σ, χ, carbides, and nitrides will inevitably precipitate at grain boundaries, phase boundaries, and in their vicinities [4–6], thus forming a Cr-depleted zone and leading to a certain intergranular corrosion sensitivity in a specific corrosion environment [7–12].

At present, methods of testing the intergranular corrosion of duplex stainless steel include the boiling acid intergranular corrosion test [13–15] and electrochemical corrosion test [16]. The former mainly provides basic data for product delivery (the qualification criteria are determined by both suppliers and consumers), while the latter is mainly used

for material research as it makes it easy to explore the corrosion mechanism. According to standards [13–15], before the boiling acid test, it is usually necessary to perform a heat treatment on dual-phase steel at a certain temperature, such as 700 °C × 0.5 h, as well as water quenching so that the material can precipitate carbides and other precipitated phases along the grain boundary to obtain more conservative test results; this is called sensitization. The double-loop electrochemical potentiokinetic reactivation method (DL-EPR method) can quickly and quantitatively detect the intergranular corrosion sensitivity of stainless steel. In recent years, the method has been widely used in duplex stainless steel [17–27]. The standard experimental medium for the DL-EPR experiment is a 0.5 mol/L H_2SO_4 + 0.01 mol/L KSCN solution [16]. In addition to KSCN [17,20–22,25], depolarizers usually include NaCl [20,21,25] and HCl [18,19,27]. For example, Lv. J. et al. studied the intergranular corrosion sensitivity of DSS2205 aged at 675 °C for different lengths of time using the DL-EPR method [17]. The results show that with an aging time ranging from 3 h to 15 h, the austenite content of the material gradually increases, the ferrite content gradually decreases, the precipitated phase gradually changes from small $M_{23}C_6$ in the initial stage of aging to the larger σ phase, and the intergranular corrosion sensitivity gradually increases. The intergranular corrosion behavior of DSS2205 at 850 °C was studied by J.L DEL A A [18], using the DL-EPR method. The results showed that with an increase in the aging time, the precipitation of the σ phase increased gradually, which increased the intergranular corrosion and uniform corrosion rates of the ferrite phase. Zhang et al. [19] used the DL-EPR method to study the intergranular corrosion resistance of dual-phase UNS S31803 steel after multi-pass welding. The results showed that the formation of chromium nitride and secondary austenite during the welding process reduced the intergranular corrosion resistance of the material. It can be seen from the above that researchers studied the intergranular corrosion performance of dual-phase steel using the DL-EPR method, mainly obtaining results indicating that the intergranular corrosion sensitivity of dual-phase steel shows an increasing trend with an increase in tempering temperature or time, and they did not use boiling acid testing for verification, lacking guidance for practical applications. The authors of this article conducted boiling acid tests on DSS2205 in different tempering states and found that corrosion rates were not completely positively correlated with tempering temperature.

In this study, the microstructure evolution of DSS2205 was studied with an increasing tempering temperature. The intergranular corrosion properties of DSS2205 following different tempering temperatures were studied using the boiling acid (65% nitric acid and 50% sulfuric acid–ferric sulfate) intergranular corrosion test and DL-EPR test. Finally, we established and discussed the correlation between the results of the boiling acid intergranular corrosion experiments and DL-EPR experiments and recommended a sensitization temperature control range for laboratory boiling acid experiments performed on DSS2205.

2. Materials and Methods

2.1. Materials

The experimental alloy was a 10 mm thick DSS2205 steel plate in the delivery state (the solid solution state; the heat treatment was conducted at 1050 °C for 1 h, and then the sample was water-quenched). The chemical composition of the alloy is shown in Table 1. The DSS2205 was tempered at different temperatures and then tested. The tempering processes were 675 °C × 1 h (marked as 1#), 700 °C × 1 h (marked as 2#), 725 °C × 1 h (marked as 3#), 750 °C × 1 h (marked as 4#), 775 °C × 1 h (marked as 5#), and 800 °C × 1 h (marked as 6#), respectively, followed by water-cooling. The solid-solution-state specimens were marked as 0#.

Table 1. Chemical composition of DSS2205 (wt.%).

C	S	P	Si	Mn	N	Cr	Ni	Mo	Fe
0.027	<0.0050	0.022	0.525	1.17	0.166	22.71	5.79	3.13	bal

2.2. Methods

According to method B of the ASTM A262-15 (2021) [15], a 50% sulfuric acid–ferric sulfate experiment was carried out, and the boiling test time was 24 h. A 65% nitric acid experiment was carried out according to ISO 3651-1:1998 [14], and the boiling test time was 48 h (some specimens were tested for 24 h as the corrosion rates were very large). Specimens showing boiling-acid intergranular corrosion were sampled along the rolling direction of the test plate, and the sampling size was 30 mm × 20 mm × 3 mm. The average rate of three specimens was taken as the final result. According to GB/T 29088-2012 [16], DL-EPR experiments were carried out on a GAMRY 1010 E electrochemical workstation (Gamry, Warminster, PA, USA) using a three-electrode system (a reference electrode was a saturated calomel electrode (SCE)). The specimen size was 10 mm × 10 mm × 10 mm. The specimen was connected to the wire and packaged with resin. The rolling surface was ground and polished as the test surface. The DL-EPR experiment was carried out in a 2 mol/L H_2SO_4 + 1.5 mol/L HCl solution at (25 ± 1) °C. The specific experimental process was as follows: First, the specimen was subjected to an open circuit potential (E_{ocp}) test for 10 min and then anodically polarized to the passivation region (E_{ocp} + 500 mV) at a scanning rate of 3.5 mV/s; it was then reversely scanned to the E_{ocp} at the same rate to determine the reactivation current (I_r) and activation current (I_a). A ratio (the reactivation rate, $R_a = I_r/I_a$) was used to characterize the intergranular corrosion sensitivity, and the higher the R_a was, the greater the intergranular corrosion sensitivity of the material. A metallographic structure observation (including a ferrite content test) was carried out using a ZEISS Oserver.Zlm metallographic microscope (ZEISS, Oberkochen, Germany). The erosion agent was a sodium sulfite hydrochloric acid aqueous solution, and the average value of the ferrite content test was taken at five positions. Transmission electron microscopy (TEM) specimens were formed by double spray perforation after mechanical pre-thinning. They were cooled using liquid nitrogen, and the temperature was lower than −20 °C. TEM observations were carried out using the JEM-2100 electron microscope (JEOL, Tokyo, Japan), and the acceleration voltage was 200 Kv.

3. Results

*3.1. Boiling Acid Intergranular Corrosion Experiment*

The experimental results determined for the DSS2205 specimens in the solid solution state and different tempering states using two standard boiling acid intergranular corrosion methods are shown in Table 2. The results show that the variations in pattern with tempering temperature of the two types of boiling acid test are consistent. The corrosion rates of the solid-solution-state specimen (0#) are the lowest, and for the specimens tempered at 675 °C–800 °C for 1 h, the tempering treatments deteriorate the intergranular corrosion resistance of the material. In the tempering range of 675 °C–725 °C, the surfaces of the specimens were pulverized after corrosion, the corrosion rates were significantly higher than those of the 0# specimens, and the corrosion resistance was seriously deteriorated. When the tempering temperature exceeds 750 °C, the corrosion resistance of the material improves again. For example, when conducting a test in a boiling 50% sulfuric acid–ferric sulfate solution for 24 h, the average rate of the DSS2205 specimen is 7.83 mm/Y when tempered at 675 °C–725 °C, while the average rate is 1.70 mm/Y when it is tempered at 750 °C–800 °C. When testing in boiling 65% nitric acid, the difference is greater than that of the boiling experiment using 50% sulfuric acid–ferric sulfate. In the tempering range of 675 °C–725 °C, due to the high corrosion rate, the standard test time had to be shortened to 24 h.

Table 2. Test results for boiling acid intergranular corrosion.

Results	Boiling Acid and Corrosion Rate (Millimeters per Year, mm/Y)	
Specimen No.	50% Sulfuric Acid–Ferric Sulfate (24 h)	65% Nitric Acid
0#	1.40	0.38 (48 h)
1#	8.44	55.57 (24 h)
2#	9.60	55.92 (24 h)
3#	5.45	54.86 (24 h)
4#	1.82	4.36 (48 h)
5#	1.47	0.51 (48 h)
6#	1.81	0.49 (48 h)

3.2. Analysis of Ferrite Content and Metallographic Structure

The ferrite content of DSS2205 specimens in the solid solution state and different tempering states is shown in Table 3, and the metallographic structure is shown in Figure 1. It can be seen that when tempering at 675 °C–725 °C for 1 h, the average content of ferrite is about 50%, which is close to that of the solid-solution-state specimen. As the tempering temperature continues to increase, the ferrite content of the material gradually decreases to 35%. As can be seen in Figure 1a, the specimen in the solid solution state has white block of austenite embedded in the black ferrite matrix. When tempering at 675 °C × 1 h, the metallographic structure is similar to that of the solid-solution-state specimen (see Figure 1b). After tempering at 700 °C × 1 h and 725 °C × 1 h, a small amount of white FeCr (σ) phase begins to precipitate along the austenite–ferrite phase boundary (see Figure 1c,d). When tempering at 750 °C × 1 h, many white σ phases are precipitated at the austenite–ferrite phase boundary and inside the ferrite phase (see Figure 1e). As the tempering temperature further increases, the generated σ phase gradually increases (see Figure 1f,g). As can be seen from the above, with an increase in the tempering temperature, the content and the size of the σ phase gradually increase with temperatures above 725 °C.
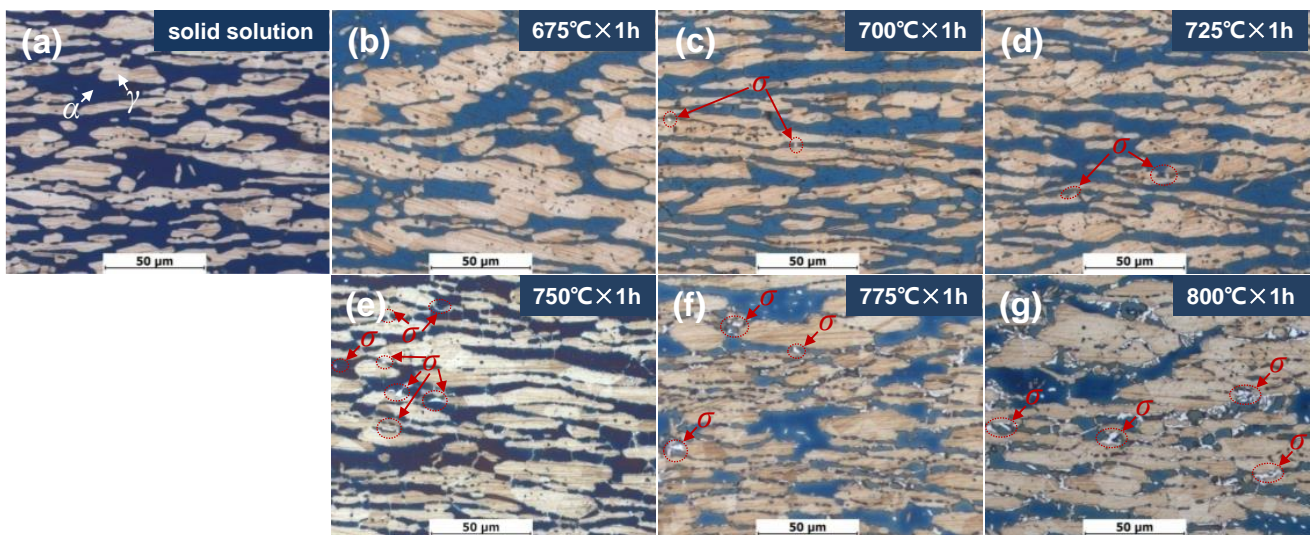
Figure 1. Metallographic morphologies of specimens in solid solution state and different tempering states: (**a**) 0#, solid solution; (**b**) 1#, 675 °C × 1 h; (**c**) 2#, 700 °C × 1 h; (**d**) 3#, 725 °C × 1 h; (**e**) 4#, 750 °C × 1 h; (**f**) 5#, 775 °C × 1 h; (**g**) 6#, 800 °C × 1 h.

Table 3. Ferrite content of DSS2205 in solid solution state and different tempering states (%).

Results Specimen No.	Points					Average
	1	2	3	4	5	
0#	50	52	54	50	45	50
1#	46	49	51	51	50	49
2#	51	47	51	53	49	50
3#	49	50	48	46	52	49
4#	44	42	43	41	45	43
5#	39	38	43	40	40	40
6#	40	37	34	34	32	35

3.3. TEM Analysis

TEM images and the precipitated phase diffraction patterns of the DSS2205 specimens in the solid solution state and different tempering states are shown in Figure 2. It can be seen in Figure 2a that the ferrite–austenite phase boundary of the solid-solution-state specimen (0#) is clean and straight, and no precipitates are produced. In Figure 2b, when tempered at 675 °C × 1 h (1#), a small amount of black precipitates are precipitated at the austenite–ferrite phase boundary of the material, which is a common σ phase in DSS2205 [4,16,17]. In Figure 2c,d,i,j, it can be seen that black strip precipitates are precipitated at the ferrite grain boundary of the specimen (2#) tempered at 700 °C × 1 h, and the result of energy dispersive spectroscopy (EDS) indicates that the precipitate should be nitride (Cr_2N). Massive black precipitates were precipitated at the austenite–ferrite phase boundary near the ferrite region; these were determined to be carbides ($Cr_{23}C_6$) from their EDS result. In addition, an Fe–Cr (σ) phase is also precipitated at the ferrite–austenite phase boundary. It can be seen from Figure 2e that the precipitated phase of the specimen tempered at 725 °C × 1 h (3#) is similar to that of the 2# specimen. A large number of black precipitates are precipitated at the ferrite–austenite phase boundary. The strip precipitates are Cr_2N. The block precipitates are σ phase, and there is also a small amount of carbides. In Figure 2f, the coarse σ phase precipitates at the ferrite phase boundary of the specimen (4#) tempered at 750 °C × 1 h are significantly larger than those of the specimens tempered at 675~725 °C, and the length reaches 2 μm. In Figure 2g, the coarse σ phase, $Cr_{23}C_6$, and a slightly smaller strip nitride are precipitated in the specimen tempered at 775 °C × 1 h (5#). The σ phase and carbides grow significantly, reaching a size of 10 μm. In Figure 2h, the precipitates of the specimen tempered at 800 °C × 1 h (6#) are mainly of the σ phase, and their size is up to 10 μm. The characteristics of the phases precipitated at each temperature are shown in Table 4. Figure 2i–m show the precipitated phase diffraction patterns of $Cr_{23}C_6$, Cr_2N, the σ phase, the ferrite matrix, and austenite in the alloy, respectively. As can be seen from the above, there are no precipitated phases in the solid solution specimen. As the tempering temperature increases, the precipitated phases gradually transform from small $M_{23}C_6$, Cr_2N, and σ phases to larger σ phases which become the main precipitated phases.

Table 4. Characteristics of precipitated phases in solid solution state and different tempering states.

Results Specimen No.	Precipitates
0#	No precipitated phase.
1#	A small amount of σ phase precipitates at the austenite–ferrite phase boundary, and a small amount of dispersed $Cr_{23}C_6$ precipitates in the ferrite grains.
2#	A small amount of σ phase precipitates at the austenite–ferrite phase boundary, $Cr_{23}C_6$ precipitates in the ferrite grain, and black strip Cr_2N precipitates at the ferrite grain boundary.
3#	At the austenite–ferrite phase boundary, strip Cr_2N precipitates, block σ phase precipitates, and a small amount of $Cr_{23}C_6$ precipitates. The size of each precipitated phase is slightly larger than that of 2#.

Table 4. *Cont.*

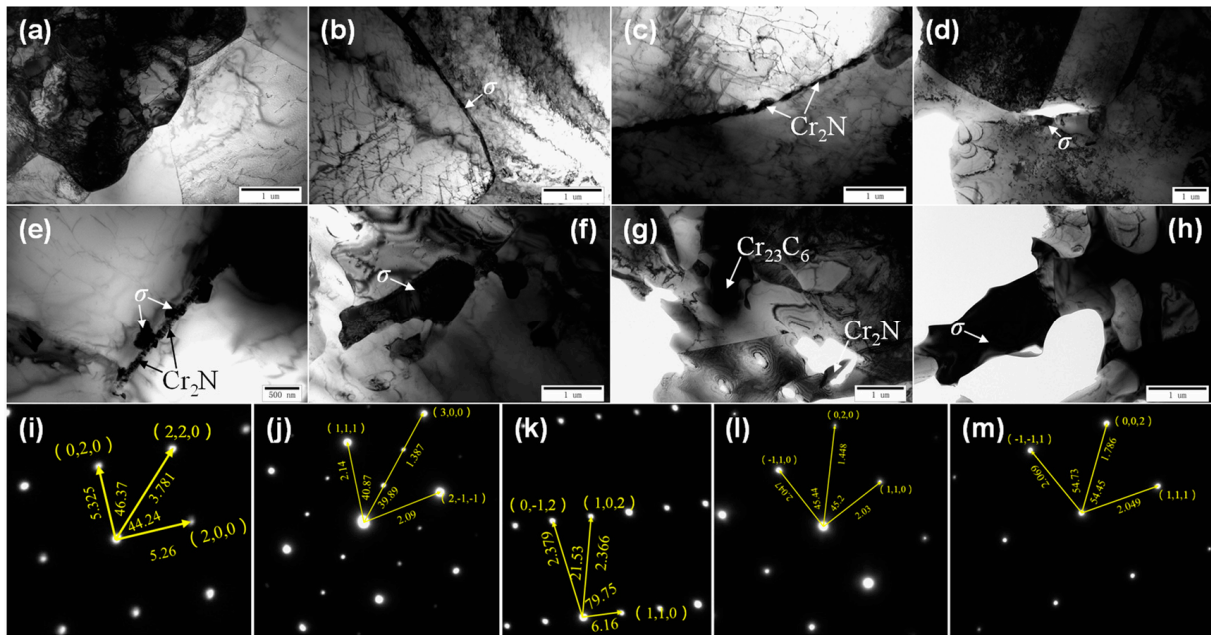| Specimen No.	Results
	Precipitates
4#	The σ phase grows significantly, and the length reaches 2 μm. Cr_2N and $Cr_{23}C_6$ also grow slightly, and their lengths are much shorter than that of the σ phase.
5#	The precipitated phases grow further, and the sizes of the σ phase and $Cr_{23}C_6$ reach 10 μm.
6#	The precipitates are mainly of the σ phase, and their size is up to 10 μm

Figure 2. TEM microstructure of specimens in solid solution state and different tempering states: (**a**) 0#, γ-α phase boundary; (**b**) 1#, γ phase boundary –σ phase; (**c**) 2#, α phase boundary—Cr_2N; (**d**) 2#, γ phase boundary, carbide; (**e**) 3#-γ-α phase boundary, nitride +σ phase; (**f**) 4#, σ phase; (**g**) 5#, σ phase, $Cr_{23}C_6$ and Cr_2N; (**h**) 6#, σ phase; (**i**) $Cr_{23}C_6$ diffraction spot; (**j**) Cr_2N diffraction spot; (**k**) σ phase diffraction spot; (**l**) ferrite diffraction spot; (**m**) austenite diffraction spot.

3.4. DL-EPR Experment

Figure 3 shows the DL-EPR curves of the DSS2205 specimens in the solid solution state and different tempering states, and the I_a and I_r values are shown in Table 5. Figure 4 shows the surface morphologies of the specimens after the DL-EPR experiment. In Figure 3, all specimens have obvious passivation zones, and the I_r value of the solid solution state specimen is very small, indicating that intergranular corrosion almost does not occur. In the range of 675 °C–725 °C, the reactivation rate R_a increases first and then decreases, and the maximum is 16%. When the tempering temperature reaches 750 °C, the R_a value of the DSS2205 increases rapidly, nearly reaching 30%. At 800 °C, the R_a value reaches 48.2%, and the I_r value is close to the I_a value of the solid-solution-state specimen, which indicates that a large range of uniform corrosion occurs when the material is reactivated.

Table 5. Test results of DL-EPR test in solid solution state and different tempering states.

Specimen No.	Results	Electrochemical Parameters		
		$I_a/mA·cm^{-2}$	$I_r/mA·cm^{-2}$	$R_a/\%$
0#		11.5	0.012	0.10
1#		13.5	0.67	4.9
2#		16.8	2.7	16.0
3#		16.3	1.9	11.6

Table 5. *Cont.*

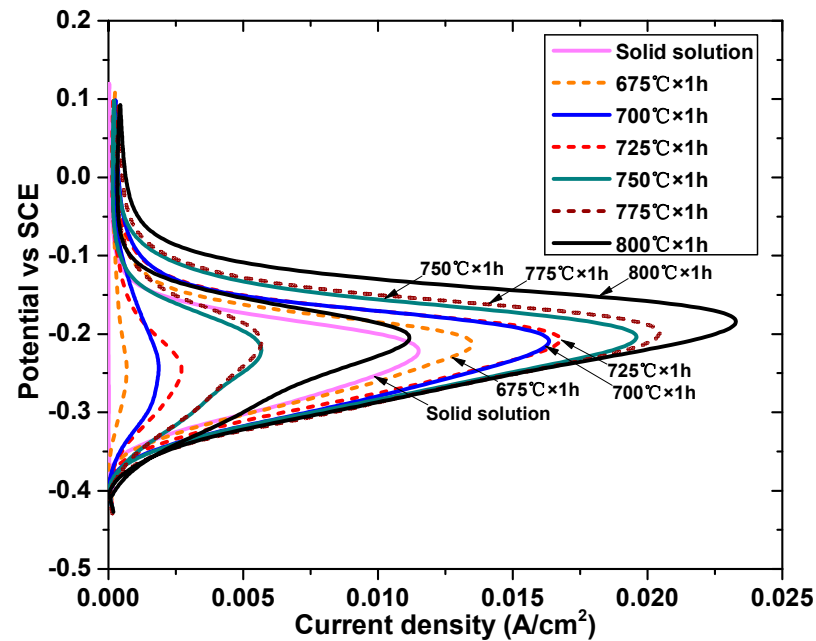| Specimen No.	Results	Electrochemical Parameters		
		$I_a/mA·cm^{-2}$	$I_r/mA·cm^{-2}$	$R_a/\%$
4#		19.6	5.6	28.5
5#		20.5	5.6	27.3
6#		23.2	11.2	48.2

Figure 3. DL-EPR curves of specimens in solid solution state and different tempering states. (SCE: saturated calomel electrode).
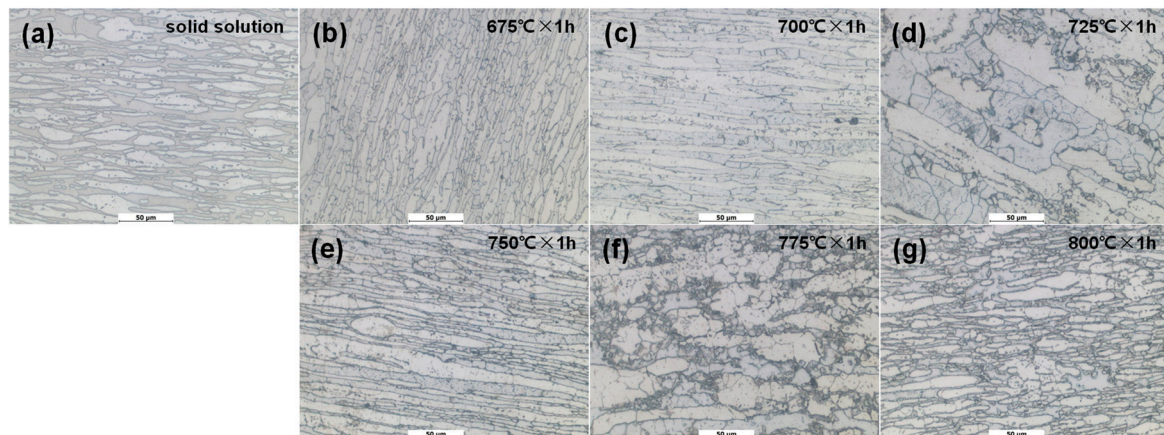

Figure 4. Morphologies of specimens after DL-EPR experiment in solid solution state and different tempering states: (**a**) 0#, solid solution; (**b**) 1#, 675 °C × 1 h; (**c**) 2#, 700 °C × 1 h; (**d**) 3#, 725 °C × 1 h; (**e**) 4#, 750 °C × 1 h; (**f**) 5#, 775 °C × 1 h; (**g**) 6#, 800 °C × 1 h.

It can be seen from Figure 4 that there is no obvious grain boundary-coarsening phenomenon in the 0# specimen (Figure 4a). Corrosion occurs at the local grain boundary of the specimen tempered at 675°C × 1 h (1# specimen in Figure 4b). The corrosion of the specimens tempered at 700 °C × 1 h (2#) and 725 °C × 1 h (3#) is aggravated, and a large number of black areas formed by corrosion appear (shown in Figure 4c,d). As the temperature continues to rise to 750 °C and above, the corrosion area of the specimen further increases, and a large area of corrosion occurs at the cluster σ phase boundary

(shown in Figure 4e–g).As can be seen from the above, the solid-solution-state specimen (0#) does not reveal intergranular corrosion, and as the tempering temperature increases, intergranular corrosion gradually intensifies.

4. Analysis and Discussion

The results show that the second phases such as σ, χ, R, π, carbides, and nitrides are precipitated in DSS2205 material during isothermal aging at 300~1000 °C, which seriously affects the performance of dual-phase steel [6,8,10–12]. From the results of this study, it can be seen that when tempering at 750 °C and above for 1 h, the ferrite content of dual-phase steel gradually decreases with the increase in temperature, and the σ phase content gradually increases. From the transmission results, $M_{23}C_6$, FeCr (σ), and Cr_2N phases were precipitated during the sensitization process at 675~800 °C, indicating that the following reactions occurred in the alloy [28]: $\alpha \rightarrow \gamma_2 + \sigma$, $\alpha \rightarrow \sigma + Cr_2N$, $\alpha \rightarrow \gamma_2 + M_{23}C_6$. (α is ferrite and γ_2 is secondary austenite).With the increase in temperature, the above reactions accelerated. $M_{23}C_6$, σ, and Cr_2N are all high-Cr compounds which have a relationship of competitive precipitation in the sensitization precipitation process of DSS2205. Under the tempering condition of 675 °C × 1 h (1#), the σ phase and carbides were precipitated in DSS2205. When the temperature reached or exceeded 700 °C, the σ phase, $M_{23}C_6$, and Cr_2N were precipitated in the DSS2205. With the increase in temperature, the number and size of the σ phase increased significantly, and it became the main precipitated phase affecting the intergranular corrosion performance of the DSS2205. The effect of the σ phase on the corrosion performance of DSS2205 is mainly discussed below, and the correlation between the boiling acid intergranular corrosion experiment and the DL-EPR experiment is established and discussed.

4.1. The Effect of Tempering Temperature on Boiling Acid Intergranular Corrosion

The results of the boiling acid intergranular corrosion test show that when the tempering temperature is 675 °C–725 °C, the corrosion rates of the DSS2205 are obviously larger than when tempered at 750 °C–800 °C. In the solid solution state, there is only the ferrite–austenite phase boundary in the DSS2205, and no precipitated phases are produced. A dense passivation film is formed on the surface of the whole specimen, and the boiling acid corrosion resistance of the material is very excellent.

During isothermal tempering between 675 °C and 725 °C, σ phase, $M_{23}C_6$, and Cr_2N precipitate at the DSS2205 phase boundary and grain boundary, and a Cr-depleted zone forms around the precipitates where the passivation film is not dense. Under boiling acid conditions, a galvanic cell reaction occurs in the specimen. The uncompacted area of the passivation film acts as the anode, and the complete area of the surrounding passivation film acts as the cathode, forming a corrosion galvanic cell with a large cathode and a small anode, and the anode was rapidly dissolved. Due to the strong oxidation of nitric acid, the corrosion potential is 0.75~1 V (SCE) [15], which is usually in the over-passivation zone. After anodic corrosion occurs, the complete area of the surrounding passivation film also dissolves, and the surface of the specimen produces a pulverization phenomenon, resulting in serious uniform corrosion. The corrosion potential of 50% sulfuric acid is 0.6 V (SCE) [15], which is lower than that of nitric acid. Therefore, the corrosion rate of the nitric acid experiment is larger than that of the 50% sulfuric acid–ferric sulfate experiment.

When DSS2205 is isothermally tempered between 750 °C and 800 °C, the content of ferrite decreases, and the content of the σ phase increases significantly, which inevitably forms a Cr-depleted zone near the precipitated phases. However, due to the high tempering temperature, Cr diffuses rapidly in the ferrite, which can supplement the Cr content in the Cr-poor zone to prevent a significant decrease in the Cr content. In addition, the Cr content in the σ phase itself is relatively high, which provides strong corrosion resistance, and the corrosion rate in boiling acid is always relatively small in the two boiling acid tests. Therefore, compared with isothermal tempering between 675 °C and 725 °C, the

corrosion rates are greatly reduced. This is particularly evident in the 65% nitric acid boiling experiment.

4.2. The Effect of Tempering Temperature on DL-EPR Experiment

In the process of the DL-EPR experiment, the passivation film on the surface of the whole material was activated and dissolved during the activation potential, from Eocp scanning to the passivation potential. When the potential reached the maximum activation current I_a, the material began to passivate, the corrosion current decreased sharply, and a dense passivation film formed on the surface of the material. Meanwhile, during reverse scanning, the dense part of the passivation film did not dissolve even at the activation potential, but the thinner part of the passivation film (such as the Cr-depleted area) dissolved. As the potential increased, the corrosion current began to decrease after reaching the maximum activation current I_r. The difference between I_r and I_a is the principle of measuring the intergranular corrosion of materials.

During isothermal sensitization between 675 °C and 725 °C, more precipitated phases were produced, and a Cr-poor zone appeared, which indicated that the material had high intergranular corrosion sensitivity. When the isothermal sensitization was carried out between 750 °C and 800 °C, although the Cr-depleted region in the material decreased due to the diffusion of the Cr element, the number of grain boundaries and phase boundaries increased significantly (especially for the boundary between the σ and α phases). Evidently, different phase compositions lead to some differences in the activation potential. In the reverse scanning process, as the potential decreases, these phase boundaries are activated, so the R_a value increases significantly. Therefore, after the DL-EPR experiment, the morphologies show corrosion traces of clusters (see Figure 4e–g) which are the corrosion traces of the phase boundary between σ and α.

4.3. Analysis of Correlation between Boiling Acid Intergranular Corrosion and DL-EPR Experiment

It can be seen from the above results that the sensitivity of intergranular corrosion in the boiling acid intergranular corrosion experiment after tempering at 675 °C–725 °C for 1 h is significantly stronger than when tempered at 750 °C–800 °C for 1 h, while the DL-EPR experimental results are just the opposite, which is due to the inconsistency of the two test principles. According to Section 3.1, the corrosion potential of the boiling acid intergranular corrosion experiment is constant (0.6–1 V) and is only sensitive to the Cr-poor area. When tempering at 675 °C–725 °C, a Cr-poor area is formed around the precipitated phase, and the passivation film in this area is not dense and dissolves easily under boiling acid conditions. When continuing to increase the tempering temperature to 750 °C–800 °C, the diffusion of Cr accelerates, which can supplement the Cr content in the Cr-poor zone. When the Cr content at the grain boundary exceeds a certain value, the passivation film becomes dense and remains in a passivation state in the potential range of 0.6–1 V, resulting in a decrease in the corrosion rate [29]. According to Section 3.2, the DL-EPR experiment is a cyclic polarization test. During the process of potential changes from activation to passivation and then from passivation to activation, while the Cr-poor area dissolves, a large number of phase boundaries also dissolve due to differences in composition and electrochemical properties. Therefore, when the tempering temperature increases to 750°C–800 °C, the ferrite content decreases significantly, the ferrite-σ phase boundary increases significantly, and the R_a value also shows a rapid increasing trend. Therefore, there is a significant difference in the sensitivity order of intergranular corrosion measured by the two experimental methods with increasing temperatures.

At present, laboratory testing mainly focuses on boiling acid intergranular corrosion experiments. The sensitization treatment temperature set by both the suppliers and consumers should be below 725 °C; otherwise, incorrect intergranular corrosion results may be obtained.

5. Conclusions

(1) After isothermal tempering at 675 °C–725 °C for 1 h, the average content of ferrite in DSS 2205 is about 50%, which is close to the solid solution state. As the tempering temperature rises to 750 °C~800 °C for 1 h, the ferrite content of the material gradually decreases to 35%. $M_{23}C_6$, FeCr (σ), and Cr_2N phases are precipitated in DSS2205 between 675 °C and 800 °C, and the content of the σ phase increases significantly at temperatures above 750 °C.

(2) During the boiling acid intergranular corrosion test, when the tempering temperature is between 675 °C and 725 °C, the average corrosion rates of DSS2205 are much larger than when it is tempered between 750 °C and 800 °C. For example, in a 50% sulfuric acid–ferric sulfate solution boiling for 24 h, the average corrosion rate of DSS2205 is 7.83 mm/Y when it is tempered at 675 °C–725 °C, while the average rate is 1.70 mm/Y when it is tempered at 750 °C–800 °C. In the DL-EPR experiment, when the tempering temperature is between 675 °C and 800 °C, the intergranular corrosion sensitivity of DSS2205 gradually increases with an increase in the tempering temperature.

(3) The degrees of sensitivity of DSS2205 to intergranular corrosion in boiling acid experiments and DL-EPR experiments at a tempering temperature of 675 °C–800 °C differ from each other. The boiling acid experiment is suitable for the determination of the intergranular corrosion tendency of the 2205 alloy with less precipitation of the σ phase.

Author Contributions: Validation, J.Z.; Formal analysis, X.L. (Xiaoyong Liu); Investigation, W.Z. and X.Y.; Resources, X.Z. (Xiaoqin Zha); Data curation, X.Z. (Xinyao Zhang); Writing—original draft, X.L.; Writing—review & editing, X.L. (Xianfu Luo); Supervision, K.F. All authors have read and agreed to the published version of the manuscript.

Institutional Review Board Statement: Not applicable.

Informed Consent Statement: Not applicable.

Data Availability Statement: The data presented in this study are available on request from the corresponding author.

Conflicts of Interest: The authors declare no conflicts of Interest.

References

1. Zha, X.Q.; Xiong, Y.; Zhou, T.; Ren, Y.F.; Hei, P.H.; Zhai, Z.L.; Kömi, J.; Huttula, M.; Cao, W. Impacts of Stress Relief Treatments on Microstructure, Mechanical and Corrosion Properties of Metal Active-GasWelding Joint of 2205 Duplex Stainless Steel. *Materials* **2020**, *13*, 4272. [CrossRef] [PubMed]

2. Mampuya, M.B.; Umba, M.C.; Mutombo, k.; Olubambi, P.A. Effect of heat treatment on the microstructure of duplex stainless steel 2205. *Mater. Today Proc.* **2021**, *38*, 1107–1112. [CrossRef]

3. Ran, Q.X.; Guo, J.Y.; Zhao, Z.L.; Duan, B.Y.; Fang, L.N.; Li, L. Study on Microstructure and Corrosion Resistance of Duplex Stainless Steel 2205 in Real Seawater Rich containing Mold. *Int. J. Electrochem. Sci.* **2022**, *17*, 220723. [CrossRef]

4. Li, J.; Du, C.W.; Liu, Z.Y.; Li, X.G.; Liu, M. Effect of microstructure on the corrosion resistance of 2205 duplex stainless steel. Part 1: Microstructure evolution during isothermal aging at 850 °C and evaluation of anticorrosion properties by methods of cyclic potentiodynamic polarization and electrochemical impedance tests. *Constr. Build. Mater.* **2018**, *189*, 1286–1293.

5. Haghdadi, N.; Ledermueller, C.; Chen, H.S.; Chen, Z.B.; Liu, Q.; Li, X.P.; Rohrer, G.; Liao, X.Z.; Ringer, S.; Primig, S. Evolution of microstructure and mechanical properties in 2205 duplex stainless steels during additive manufacturing and heat treatment. *Mater. Sci. Eng. A* **2022**, *835*, 142695. [CrossRef]

6. Li, S.X.; Ren, X.P.; Tong, J.G.; Hou, H.L. Precipitation law of σ phase in 2205 duplex stainless steel. *Chin. J. Eng.* **2015**, *37*, 312–316.

7. Gao, L.Q.; Zhang, X.Y.; Zha, X.Q.; Zhang, X.Y. Effect of Mechanical Shock Treatment on Microstructure and Corrosion Properties of Manual Argon Arc Welding Joints of 2205 Duplex Stainless Steel. *Materials* **2022**, *15*, 3230. [CrossRef] [PubMed]

8. Khan, M.S.; Yang, C.G.; Pan, H.B.; Yang, K.; Zhao, Y. The effect of high temperature aging on the corrosion resistance, mechanical property and antibacterial activity of Cu-2205 DSS. *Colloids Surf. B Biointerfaces* **2022**, *211*, 112309.

9. He, Z.X.; Zhao, Y.; Fu, J.; Chen, F.G.; Chen, G.Q.; Qin, Y.H. Effect of Alternating Magnetic Field on the Organization and Corrosion Resistance of 2205 Duplex Stainless Steel Narrow-Gap Laser-MIG Hybrid Weld Head. *Coatings* **2023**, *13*, 2000. [CrossRef]

10. Luo, X.F.; Guo, Z.Y.; Zhang, H.K.; Zhang, W.L.; Liu, X.Y.; Zha, X.Q. Crack determination and influencing factors analysis of intergranular corrosion test of 2205 duplex stainless steel. *Dev. Appl. Mater.* **2020**, *35*, 36–42.
11. Shen, K.L.; Jiang, W.C.; Sun, C.; Wan, Y.; Zhao, W.M.; Sun, J.B. Insight into microstructure, microhardness and corrosion performance of 2205 duplex stainless steel: Effect of plastic pre-strain. *Corros. Sci.* **2023**, *210*, 110847. [CrossRef]
12. Zhu, L.Y.; Wu, J.J.; Wang, P.; Zhang, D.; Li, C.; Gao, Y.H.; Wang, W.K. The effects of σ phase on localized corrosion of 2205 duplex stainless steel in the presence of Pseudomonas aeruginosa. *Corros. Sci.* **2024**, *232*, 112042. [CrossRef]
13. *GB/T 4334-2020*; Corrosion of Metals and Alloys—Test Methods for Intergranular Corrosion of Austenitic and Ferritic-Austenitic (Duplex) Stainless Steels. Standardization Administration of China: Beijing, China, 2020.
14. *ISO 3651-1-1998*; Determination of Resistance to Intergranular Corrosion of Stainless Steels—Part 1: Austenitic and Ferritic-Austenitic (Duplex) Stainless Steels—Corrosion Test in Nitric Acid Medium by Measurement of Loss in Mass (Huey Test). ISO: Geneva, Switzerland, 1998.
15. *ASTM A262-15(2021)*; Standard Practices for Detecting Susceptibility to Intergranular Attack in Austenitic Stainless Steels. ASTM: West Conshohocken, PA, USA, 2021.
16. *GB/T 29088-2012*; Corrosion of Metals and Alloys, Electrochemical Potentiokinetic Reactivation (EPR) Measurement Using the Double Loop Method. Standardization Administration of China: Beijing, China, 2012.
17. Lv, J.; Liang, T.; Dong, L.; Chen, W. Influence of sensitization on microstructure and passive property of AISI 2205 duplex stainless steel. *Corros. Sci.* **2016**, *104*, 144–151.
18. Abra-Arzola, J.D.; García-Rentería, M.; Cruz-Hernández, V.; García-Guerra, J.; Martínez-Landeros, V.; Falcón-Franco, L.; Curiel-López, F. Study of the effect of sigma phase precipitation on the sliding wear and corrosion behaviour of duplex stainless steel AISI 2205. *Wear* **2018**, *400–401*, 43–51. [CrossRef]
19. Zhang, Y.Q.; Cheng, S.H.; Wu, S.J.; Chen, F.J. The evolution of microstructure and intergranular corrosion resistance of duplex stainless steel joint in multi-pass welding. *J. Mater. Process. Tech.* **2020**, *277*, 116471. [CrossRef]
20. Jeon, S.H.; Kim, H.J.; Parh, Y.S. Effects of inclusions on the precipitation of chi phases and intergranular corrosion resistance of hyper duplex stainless steel. *Corros. Sci.* **2014**, *87*, 1–5. [CrossRef]
21. Ortiz, N.; Curiel, F.F.; López, V.H.; Ruiz, A. Evaluation of the intergranular corrosion susceptibility of UNS S31803 duplex stainless steel with thermoelectric power measurements. *Corros. Sci.* **2013**, *69*, 236–244. [CrossRef]
22. Deng, B.; Jiang, Y.M.; Xu, J.L.; Sun, T.; Gao, J.; Zhang, L.H.; Zhang, W.; Li, J. Application of the modified electrochemical potentiodynamic reactivation method to detect susceptibility to intergranular corrosion of a newly developed lean duplex stainless steel LDX2101. *Corros. Sci.* **2010**, *52*, 969–977. [CrossRef]
23. Hong, J.F.; Han, D.; Tan, H.; Li, J.; Jiang, Y.M. Evaluation of aged duplex stainless steel UNS S32750 susceptibility to intergranular corrosion by optimized double loop electrochemical potentiokinetic reactivation method. *Corros. Sci.* **2013**, *68*, 249–255. [CrossRef]
24. Shi, Y.H.; Cui, S.W.; Zhu, T.; Gu, S.; Shen, X. Microstructure and intergranular corrosion behavior of HAZ in DP-TIG welded DSS joints. *J. Mater. Process. Technol.* **2018**, *256*, 254–261. [CrossRef]
25. Rajkumar, M.; Babu, S.P.K.; Nagaraj, T.A. Intergranular corrosion characteristics of niobium stabilized 27Cr-7Ni-Mo-W-N cast hyper duplex stainless steel. *Mater. Today Proc.* **2020**, *27*, 2551–2555. [CrossRef]
26. Kim, H.J.; Jeon, S.H.; Kim, S.T.; Lee, I.S.; Park, Y.S.; Kim, K.T.; Kim, Y.S. Investigation of the sensitization and intergranular corrosion of tube-to-tubesheet welds of hyper duplex stainless steel using an electrochemical reactivation method. *Corros. Sci.* **2014**, *87*, 60–70. [CrossRef]
27. Gong, J.; Jiang, Y.M.; Deng, B.; Xu, J.L.; Hu, J.P.; Li, J. Evaluation of intergranular corrosion susceptibility of UNS S31803 duplex stainless steel with an optimized double loop electrochemical potentiokinetic reactivation method. *Electrochim. Acta* **2010**, *55*, 5077–5083. [CrossRef]
28. Iacoviello, F.; Di Cocco, V.; Franzese, E. Integranular corrosion susceptibility analysis in austeno-ferritic (duplex) stainless steels. *Fatigue Fract. Eng. Mater. Struct.* **2017**, *3*, 276–282. [CrossRef]
29. Jiang, J.Y.; Wang, D.Q.; Chu, H.Y.; Ma, H.; Liu, Y.; Gao, Y.; Shi, J.J.; Sun, W. The Passive Film Growth Mechanism of New Corrosion-Resistant Steel Rebar in Simulated Concrete Pore Solution: Nanometer Structure and Electrochemical Study. *Materials* **2017**, *10*, 412. [CrossRef] [PubMed]